

A Modular Pragmatic Architecture for Multiuser MIMO with Array-Fed RIS

Krishan K. Tiwari, Giuseppe Caire
 Technische Universität Berlin, 10587 Berlin, Germany
 Email addresses: lastname@tu-berlin.de

Abstract—We propose a power- and hardware-efficient, pragmatic, modular, multiuser/multibeam array-fed RIS architecture particularly suited to operate in very high frequency bands (high mmWave and sub-THz), where channels are typically sparse in the beamspace and line-of-sight (LOS) is required to achieve an acceptable received signal level. The key module is an active multi-antenna feeder (AMAF) with a small number of active antennas placed in the near field of a RIS with a much larger number of passive controllable reflecting elements. We propose a pragmatic approach to obtain a steerable beam with high gain and very low sidelobes. Then, K independently controlled beams can be achieved by stacking K of such AMAF-RIS modules. Our analysis takes in full account: 1) the near-end crosstalk (NEXT) between the modules, 2) the far-end crosstalk (FEXT) due to the sidelobes; 3) a thorough energy efficiency comparison with respect to conventional *active arrays* with the same beamforming performance. Overall, we show that the proposed architecture is very attractive in terms of spectral efficiency, ease of implementation (hardware complexity), and energy efficiency.

Index Terms—Reflective intelligent surface (RIS), reflectarrays, multiuser MIMO, mmWave and sub-THz communications, line of sight MIMO.

I. INTRODUCTION

Wireless communication in the millimeter wave (mmWave) and sub-THz frequency bands has garnered significant attention recently due to the promise of high data rates and ultra-low latency [1]. At these frequencies, traditional wide-angle antennas and non-line-of-sight (NLOS) propagation are inadequate, prompting the use of large aperture antenna arrays for highly directional line-of-sight (LOS) propagation. This enables applications like wireless fronthaul, fixed point-to-multipoint wireless access (FWA), and LOS multiuser MIMO with highly directional beams [2]. However, the complexity and power efficiency of large beamsteering active arrays remain problematic. To address this, innovative antenna configurations like Reflectarrays and Reflective Intelligent Surfaces (RIS) have been explored [3]–[5]. RIS, in particular, has been studied to modify wireless channels, but its effectiveness in the far field is limited by signal strength unless the RIS size is impractically large, even for indoor applications [6].

From the Friis transmission equation [7, eq. (2-119)],

$$\frac{P_{rx}}{P_{tx}} = \frac{A_{tx}A_{rx}}{(d\lambda)^2}, \quad (1)$$

where λ , d , P , and A denote the carrier wavelength, distance, power, and antenna (effective) aperture, respectively. The suffixes $_{rx}$ and $_{tx}$ denote receiver and transmitter. We see that for

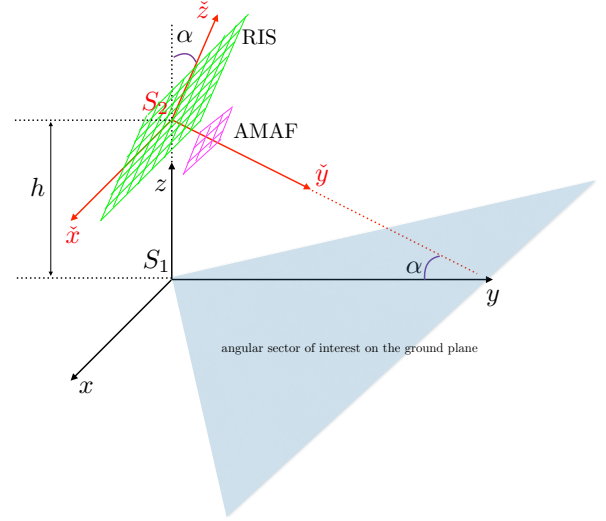


Fig. 1: 3D geometry, conceptual (not to scale).

fixed antenna size and decreasing λ , extreme power efficiency can be achieved. To maximize energy efficiency, and to reduce the hardware complexity of very large array antennas, we propose using RIS in a reflectarray configuration in the near field of a small active multi-antenna feeder (AMAF) configured along the principal eigenmode of the AMAF-RIS propagation matrix. In this work, we build on our previous work [5] and present a full-dimensional (3D) model with planar RIS and AMAF arrays for terrestrial mmWave/sub-THz picocell base station applications, where the RIS is mechanically downtilted pointing to the picocell centroid on the ground, see Fig. 1. Recall that the aperture efficiency of a planar patch array is much higher (90% and more) than that of “legacy” feed horn (51% for optimum pyramidal horns) widely used for space feeding, which in turn alleviates the aperture blockage issue in the front illumination of reflectarrays. This motivates us to consider the AMAF instead of a horn as in traditional reflectarrays. Our mathematical model-based work encompasses also the back illumination [8] which has a reflected geometry with respect to the front illumination, since under the idealized assumption made in our work the two models are identical. Whether front or back illumination is preferable depends on the blocking effect on the far field radiation pattern versus the power waste due to material absorption of the propagation through the metasurface [8]. These aspects are design/material dependent and go beyond the scope of this paper.

II. THE AMAF-RIS MODULE: DESIGN PRINCIPLES

As in Fig. 1, we define two coordinate systems. S1 has its origin on the ground plane x-y. S2 has its origin in the center of the RIS, positioned at $(0, 0, h)$ with respect to the S1 system, and is downtilted by a rotation of $-\alpha$ in the z-y plane. Let $\mathbf{i} = (1, 0, 0)^T, \mathbf{j} = (0, 1, 0)^T, \mathbf{k} = (0, 0, 1)^T$ denote the three versors of S1 in the coordinate system S1, and $\check{\mathbf{i}} = (1, 0, 0)^T, \check{\mathbf{j}} = (0, 1, 0)^T, \check{\mathbf{k}} = (0, 0, 1)^T$ denote the three versors of S2 in the coordinate system S2. A S1 point $\mathbf{p} = p_x\mathbf{i} + p_y\mathbf{j} + p_z\mathbf{k}$ can be expressed in S2 Cartesian coordinates $\check{\mathbf{p}} = \check{p}_x\check{\mathbf{i}} + \check{p}_y\check{\mathbf{j}} + \check{p}_z\check{\mathbf{k}}$ by

$$\check{\mathbf{p}} = \begin{bmatrix} 1 & 0 & 0 \\ 0 & \cos(\alpha) & -\sin(\alpha) \\ 0 & \sin(\alpha) & \cos(\alpha) \end{bmatrix} (\mathbf{p} - (0, 0, h)^T). \quad (2)$$

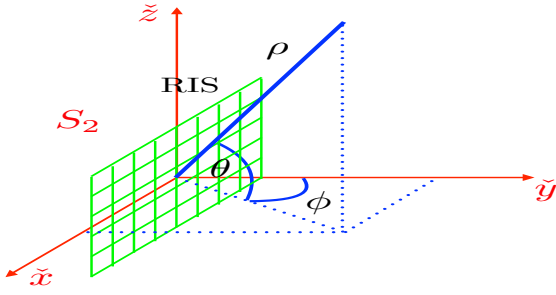


Fig. 2: Spherical coordinates definition for the RIS coordinate system S2.

For the S2 spherical coordinates in Fig. 2, the RIS boresight direction $\check{\mathbf{j}}$ corresponds to the angles $\phi = 0, \theta = 0$, and this is a line tilted down and impinging the picocell centroid on the ground plane (S1 x-y plane) by an angle α (see Fig. 1). Hence, a point of $\check{\mathbf{p}}$ in S2 with spherical coordinates (ρ, ϕ, θ) has $\check{p}_x = \rho \sin \phi \cos \theta, \check{p}_y = \rho \cos \phi \cos \theta, \check{p}_z = \rho \sin \theta$. This, along with (2), maps any S1 ground plane point to a far-field direction (ϕ, θ) and a range ρ with respect to the RIS. In the following, all lengths are normalized by $\lambda/2$.

A. RIS Array and Far-Field Array Response

A planar wavefront impinging a standard rectangular array (SRA) RIS at an angle (ϕ, θ) has normal vector given by

$$\mathbf{n}(\phi, \theta) = (\sin \phi \cos \theta, \cos \phi \cos \theta, \sin \theta)^T. \quad (3)$$

The planar wave propagation phase delay (complex phasor term) of the (n, m) element of the RIS is given by

$$a_{n,m}(\phi, \theta) = \exp(-j\pi\check{\mathbf{p}}_{n,m}^T \mathbf{n}(\phi, \theta)). \quad (4)$$

where $\check{\mathbf{p}}_{n,m}$ is the position of the (n, m) RIS elements in the system S2. We use axisymmetric model for the RIS and the AMAF patch elements (having a 3 dB beamwidth of 90° and the power gain of 6 dBi) given by $G_{\text{patch}}(\theta, \phi) = 4 \cos^2(\psi)$, where ψ is the angle of the direction (ϕ, θ) with respect to the patch broadside, i.e., the S2 y-axis. Noticing that $\cos(\psi) = \mathbf{n}(\phi, \theta) \cdot (0, 1, 0)^T = \cos \phi \cos \theta$, we have

$$G_{\text{patch}}(\phi, \theta) = 4 (\cos \phi \cos \theta)^2. \quad (5)$$

Assuming a RIS excitation by the AMAF such that the complex signal at each element is $u_{n,m}$, the RIS can further impose a phase rotation $w_{n,m} = e^{j\mu_{n,m}}$ for each n, m element. Hence, the resulting far-field radiation pattern as a function of the angle direction (ϕ, θ) is given by

$$G(\phi, \theta) = G_{\text{patch}}(\phi, \theta) \left| \sum_{n=0}^{N_x-1} \sum_{m=0}^{N_z-1} w_{n,m} u_{n,m} a_{n,m}^*(\phi, \theta) \right|^2. \quad (6)$$

We also notice that, without loss of generality, we can incorporate the phase of $u_{n,m}$ into $w_{n,m}$. Hence, without loss of generality, we can replace $u_{n,m}$ by its magnitude $|u_{n,m}|$. For convenience, we define the ‘‘tapered’’ RIS weights $\tilde{w}_{n,m}(\phi, \theta) = |u_{n,m}|w_{n,m}$. Collecting $\{a_{n,m}(\phi, \theta)\}$ and $\{\tilde{w}_{n,m}\}$ into two $N_p \times 1$ vectors $\mathbf{a}(\phi, \theta)$ and $\check{\mathbf{w}}$, (6) can be compactly written as

$$G(\phi, \theta) = 4 (\cos \phi \cos \theta)^2 |\mathbf{a}(\phi, \theta)^H \check{\mathbf{w}}|^2. \quad (7)$$

B. AMAF-RIS Illumination and Beam-Steering

We focus now on the illumination, i.e., how to obtain a suitable (complex) amplitude profile $\{u_{n,m}\}$ induced by the AMAF on the RIS surface. The AMAF is formed by $N_a = N_h N_v$ active elements arranged in a $N_h \times N_v$ SRA and placed at a distance F from the RIS with $N_p = N_x N_z$ elements arranged in a $N_x \times N_z$ SRA. For convenience, we enumerate the RIS and the AMAF elements row by row using indices $k \in \{0, \dots, N_p - 1\}$ and $\ell \in \{0, \dots, N_a - 1\}$, respectively. Letting $r_{k,\ell}$ denote the distance between the k -th RIS element and the ℓ -th AMAF element, and letting $(\varphi_{k,\ell}, \vartheta_{k,\ell})$ the angle at which they see each other with respect to their own normal (boresight) direction, narrowband near-field AMAF-RIS propagation matrix $\mathbf{T} \in \mathbb{C}^{N_p \times N_a}$ has entries

$$T_{k,\ell} = \frac{\sqrt{E_A(\varphi_{k,\ell}, \vartheta_{k,\ell}) E_R(\varphi_{k,\ell}, \vartheta_{k,\ell})}}{2\pi r_{k,\ell}} e^{-j\pi r_{k,\ell}}, \quad (8)$$

where $E_A(\varphi, \vartheta) = E_R(\varphi, \vartheta) = G_{\text{patch}}(\varphi, \vartheta)$ in this work.

Consider the Singular Value Decomposition (SVD) of $\mathbf{T} = \mathbf{U}\mathbf{S}\mathbf{V}^H$ where $\mathbf{U} \in \mathbb{C}^{N_p \times N_p}$ and $\mathbf{V} \in \mathbb{C}^{N_a \times N_a}$ are unitary matrices and $\mathbf{S} \in \mathbb{C}^{N_p \times N_a}$ is a diagonal matrix containing ordered singular values $\sigma_1, \sigma_2, \dots, \sigma_{N_a}$. Letting $\mathbf{u}_\ell, \mathbf{v}_\ell$ denotes the ℓ^{th} columns \mathbf{U}, \mathbf{V} , respectively, any AMAF weight vector $\mathbf{b} \in \mathbb{C}^{N_a}$ can be written as $\mathbf{b} = \sum_{\ell=1}^{N_a} \mu_\ell \mathbf{v}_\ell$ with the transmit power normalization $\sum_{\ell=1}^{N_a} |\mu_\ell|^2 = 1$. This results in the complex amplitude profile $\mathbf{u} = \mathbf{T}\mathbf{b} = \sum_{\ell=1}^{N_a} \sigma_\ell \mu_\ell \mathbf{u}_\ell$. As an effective pragmatic choice of the AMAF weight vector, we let $\mathbf{b} = \mathbf{v}_1$, referred to as *principal eigenmode* (PEM) design. This results in the ‘‘template’’ RIS weight vector $\check{\mathbf{w}}_0 = \sigma_1 \mathbf{u}_1 \odot e^{-j\angle \mathbf{u}_1}$ with all elements in \mathbb{R}_+ , corresponding to a beam pointing in the boresight direction of the RIS.¹ For example, Fig. 3 shows the template beam ground footprint for a 16x16 RIS fed by a 2x2 AMAF at a 20m high base station mast with $\alpha = 37.37^\circ$ as detailed in Section IV. The PEM

¹Here $\angle \mathbf{u}_1$ is the vector of phases of \mathbf{u}_1 , \exp is applied componentwise, and \odot is elementwise product.

design yields the RIS amplitude taper in see Fig. 4, yielding -35 dB sidelobes and 28 dBi gain. Beamsteering of the template beam to a desired direction (ϕ_0, θ_0) is obtained by imposing a linear phase gradient in the form $\mathbf{w} = \mathbf{a}(\phi_0, \theta_0) \odot \tilde{\mathbf{w}}_0$.

Remark 1: It is important to notice that the AMAF weight vector depends only on the AMAF-RIS geometry of the basic module, and not on the beam-steering. In a multi-beam multiuser setting, only the steering depends on the user channels and can be adapted by changing the RIS phases while the AMAF configuration remains fixed. \diamond

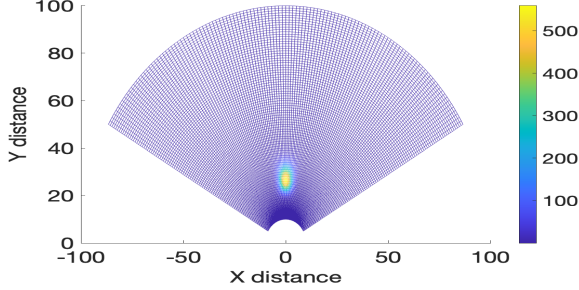


Fig. 3: Ground footprint (coordinate system S1) of the RIS PEM spotbeam pointing at the RIS boresight (coordinate system S2), for a 16×16 RIS with 2×2 AMAF at distance $F = 6$.

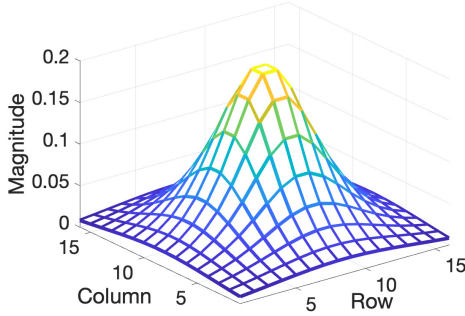


Fig. 4: RIS PEM amplitude profile for a 16×16 RIS with 2×2 AMAF at distance $F = 6$.

III. MULTI-BEAM MULTIUSER MIMO

Following the “One Stream Per Subarray” (OSPS) approach to multiuser MIMO [9], we consider stacking $K > 1$ AMAF-RIS basic modules with minimal separation of length $\lambda/2$ (i.e., unit separation in normalized distance) for maximum space utilization.

The global matrix $\mathbf{T} \in \mathbb{C}^{KN_p \times KN_a}$ for the stacked modules can be written as a $K \times K$ block matrix where each block $\mathbf{T}_{i,j} \in \mathbb{C}^{N_p \times N_a}$ models the propagation between the j -th AMAF and the i -th RIS and is calculated from (8). We define also $\mathbf{W}_i = \text{diag}(\mathbf{w}_i)$, for the i -th RIS phase-only weight vector (not inclusive of the amplitude taper as in $\tilde{\mathbf{w}}$) and $\mathbf{b}_j \in \mathbb{C}^{N_a \times 1}$ to be the j -th AMAF weight vector. Defining the block-diagonal matrices $\mathbf{W} = \text{diag}(\mathbf{W}_i : i = 1, \dots, K)$ and $\mathbf{B} = \text{diag}(\mathbf{b}_j : j = 1, \dots, K)$, the global transmission matrix $\mathbf{N} \in \mathbb{C}^{KN_p \times K}$ from the K baseband antenna ports

(each driving one AMAF) and the RIS reflecting elements is given by the block matrix $\mathbf{W}\mathbf{T}\mathbf{B}$ whose i, j -th block is given by

$$[\mathbf{N}]_{i,j} = [\mathbf{W}\mathbf{T}\mathbf{B}]_{i,j} = \mathbf{W}_i \mathbf{T}_{i,j} \mathbf{b}_j \in \mathbb{C}^{N_p \times 1}. \quad (9)$$

Since the K modules are identical, we have that $\mathbf{T}_{1,1} = \dots = \mathbf{T}_{K,K}$. Our pragmatic design uses the PEM approach for each module, i.e., $\mathbf{b}_j = \mathbf{v}_1$ for all $j = 1, \dots, K$. Hence, the diagonal blocks $\mathbf{N}_{j,j}$ (in isolation) produce radiation patterns as seen before, i.e., independently steered versions of the basic weight vector $\tilde{\mathbf{w}}_0$. The off-diagonal blocks $\mathbf{N}_{i,j}$ for $i \neq j$ capture the effect of the near-end crosstalk (NEXT) between the modules. Fortunately, given the good tapered profile of the PEM design (see Fig. 4), it turns out that the NEXT is essentially negligible even for unit separation between the modules.

We consider a multiuser MIMO scenario where the base station (BS) is equipped with K AMAF-RIS modules and serves multiple users located in the coverage area (see Fig. 1). The downlink scheduler chooses groups of K users to be served on the same time slot by spatial multiplexing. The resulting LOS baseband channel matrix $\mathbf{H} \in \mathbb{C}^{K \times K}$ between the K BS antenna ports and the K (far-field) users is given by

$$\mathbf{H} = \mathbf{A}^H \mathbf{W}\mathbf{T}\mathbf{B} \quad (10)$$

where

$$\mathbf{A} = 2 [\cos\phi_1 \cos\theta_1 \mathbf{a}(\phi_1, \theta_1), \dots, \cos\phi_K \cos\theta_K \mathbf{a}(\phi_K, \theta_K)] \quad (11)$$

is the $KN_p \times K$ matrix containing the steering vectors whose elements are given by (4) from the overall stacked RIS array to the K users, where each user k is seen at an angle (ϕ_k, θ_k) with respect to the RIS S2 coordinate system. Each k -th steering vector is weighted by $\sqrt{G_{\text{patch}}(\phi_k, \theta_k)} = 2 \cos\phi_k \cos\theta_k$ due to the RIS element directivity. The off-diagonal terms in \mathbf{H} capture the far-end crosstalk (FEXT) due to the sidelobes of the AMAF-RIS beams. Ideally, we want the matrix \mathbf{H} to be strongly diagonal-dominant which allows us to dispense with (digital) baseband signal processing techniques such as zero-forcing. This can be achieved by a) our proposed PEM design which yields very low sidelobes, and 2) by scheduling sets of K “compatible” users, which in the LOS MU-MIMO case means users with sufficient angular separation in azimuth and/or elevation. Notice that the selection of compatible (nearly mutually orthogonal) sets of users in MU-MIMO is a common practice, as currently implemented in 802.11ax MU-MIMO mode (e.g., see [10] and references therein).

The achievable communication rate of user k under Gaussian single-user capacity achieving codebooks and treating multiuser interference as noise is given by

$$R_k = \log_2 \left(1 + \frac{|H_{k,k}|^2 P_{\text{RF}}}{WN_0/L_k + \sum_{j=1, j \neq k}^K |H_{k,j}|^2 P_{\text{RF}}} \right), \quad (12)$$

bits per complex signal dimension, where $H_{k,j}$ is the (k, j) -th element of \mathbf{H} , P_{RF} is the total AMAF output RF power, N_0 is the complex baseband AWGN power spectral density, W is the

channel bandwidth, and $L_k = (\lambda/(4\pi\rho_k))^2$ is the free-space pathloss due to distance ρ_k (in meters) between user k and the BS. In the LOS condition, \mathbf{H} is deterministic, and hence any standard synchronization (carrier frequency, timing, and phase) at the user receivers can easily achieve (almost) ideal coherent detection.

IV. MU-MIMO EXAMPLE

We present a case study where the RIS and the AMAF are SRAs of size $N_x = N_z = 16$ and $N_h = N_v = 2$, respectively. We choose an empirically optimum focal length $F = 6$, chosen to strike a good balance between beam directivity, loss in the AMAF-RIS structure (captured by the value of singular-value σ_1), and height of the sidelobes. Qualitatively, if F is too small only a central portion of the RIS is illuminated by the AMAF, i.e., the elements of the RIS away from the center play no role in beamforming. If F is too large, then a large fraction of the RF power radiated by the AMAF is lost in space (and creates significant NEXT in the multi-module stacked array), since the solid angle covered by the RIS is too small and also higher FEXT due to a smaller RIS taper. In the case at hand, $F = 6$ with the PEM beamforming yields the nice tapered amplitude profile shown in Fig. 4, resulting in the template beam with footprint in Fig. 3.

We consider $K = 4$ stacked modules height $h = 20\text{m}$ on the ground, serving a sector on the ground S1 x-y plane with range between $r_{\min} = 10\text{m}$ to $r_{\max} = 100\text{m}$, azimuth ϕ from -60° to 60° . The 10m and 100m ground distances correspond to the downlook angles of $\alpha_{\max} = \text{acot}(r_{\min}/h) = 63.43^\circ$ and $\alpha_{\min} = \text{acot}(r_{\max}/h) = 11.30^\circ$, respectively, with respect to the S2 origin. Therefore, we choose the RIS mechanical downtilt angle α to be the arithmetic mean, i.e. $\alpha = 37.37^\circ$, for the optimum element factor utilization in the elevation. This downtilt angle causes the RIS normal vector to intercept the ground at distance $r = 26.19\text{ m}$, as shown in Fig. 3.

In order to ensure a minimum 0 dB² SNR to any user in the picocell, we consider the link budget of Table I. The RF feed power from the AMAF, $P_{\text{RF}} = P_T/G(\phi, \theta)$ where $G(\phi, \theta)$ is given in (7). At the cell edge, $G(\phi = 60^\circ, \theta = 26.06^\circ) = 20.7\text{ dBi}$, yielding a required AMAF RF power of $P_{\text{RF}} = 40.7\text{ dBm} - 20.7\text{ dBi} = 20\text{ dBm}$.

TABLE I: Example system specifications.

Specification	Value	Specification	Value
Carrier freq. (GHz)	100	Receive noise pow. (dBm)	-72
Cell range (m)	10 to 100	Receive SNR (dB)	0
Azimuth span (ϕ)	$\pm 60^\circ$	Receive signal power (dBm)	-72
Bandwidth W (GHz)	5	Path Loss L_{\max} (dB)	112.7
Thermal noise pow. (dBm)	-77	EIRP P_T (dBm)	40.7
Rx NF (dB)	5	RIS size ($N_x \times N_z$)	16 x 16

We consider $K = 4$ downlink data streams serving 4 users randomly distributed with azimuth $\phi \in [-60^\circ, 60^\circ]$ and range $r \in [10\text{m}, 100\text{m}]$. The scheduler chooses the K users

²Notice that an SNR of 0 dB corresponds to a channel capacity equal to 1 per complex dimension, which is approachable in practice using QPSK modulation with powerful binary LDPC coding of rate (slightly less than) 1/2. Hence, such a system is quite realistic also from a practical viewpoint.

a minimum azimuth angle separation of 15° , corresponding to the -20 dB beam contour of the template beam. Fig. 5 shows a snapshot (random realization) of 4 user positions and the corresponding ground beam footprints with ideal beam steering (i.e., by pointing the beams towards the corresponding users angles).

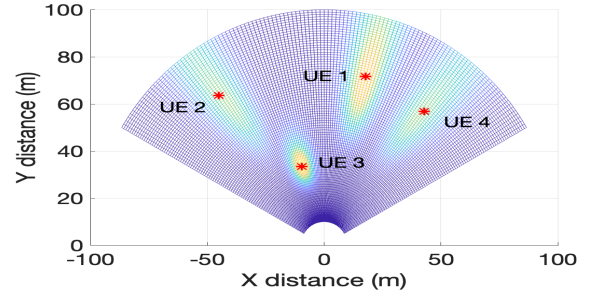


Fig. 5: Ground footprints: an example set of 4 PEM spot beams, with perfect beam pointing onto the 4 UEs.

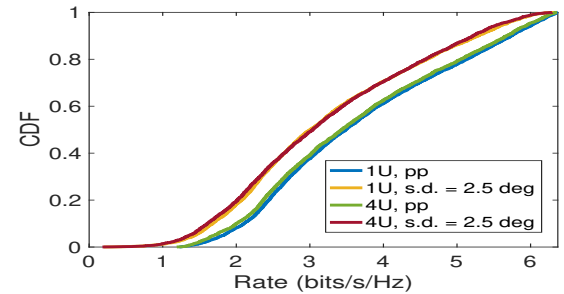


Fig. 6: Rate CDFs for the beam pointing case, with perfect pointing (pp) and with Gaussian beam pointing errors.

Fig. 6 shows the achievable rate CDF for the case of a single user (1U), and 4 users (4U), with perfect beam pointing (pp), and independent Gaussian beam pointing errors in both ϕ and θ with standard deviations of 2.5° . We find that the rate degradation due to beam pointing errors is tolerable because the beam footprints have a smooth contour, which provides some robustness to pointing errors. We see also that there is no practical degradation between the single user and the 4 users case, indicating that the FEXT/NEXT multiuser interference is effectively negligible. This means that any further hybrid precoding would yield no improvement at the cost of a much higher computational complexity in the baseband.

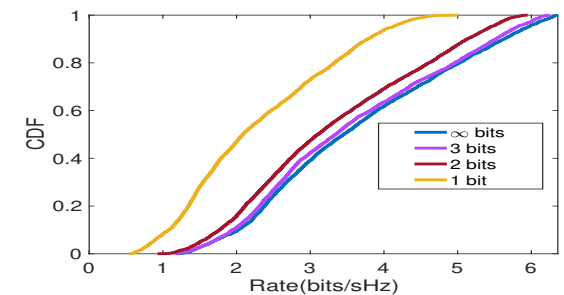


Fig. 7: Rate CDFs for the beam pointing case, with perfect pointing and RIS quantized phase-shifters.

In Fig. 7 we show the rate CDF for the same system scenario, with no pointing errors and quantized RIS phase-shifters. We used simple scalar quantization of the continuous phases, without any further complicated optimization. For 3 or more quantization bits, the rate CDF is essentially identical to the unquantized case. Nevertheless, even for just 1 bit quantization, i.e., restricting the RIS phase shifts to ± 1 , the per-user rates range from ≈ 0.5 to ≈ 5 bits/symbol, corresponding to ≈ 0.25 to ≈ 2.5 Gb/s (with $W = 5$ GHz as in Table I).

V. POWER EFFICIENCY ANALYSIS

For the same planar array dimension and beamforming radiation pattern of the proposed AMAF-RIS architecture (Arch.1), we consider a baseline architecture consisting of a constrained-fed active array (Arch.2), where each element has its own dedicated power amplifier (PA), see Fig. 8. For Arch.2 we neglect the power loss incurred by the beamforming network from the antenna port to the array elements (i.e., to the signals before the per-antenna PAs) because this operates on low-level signals and impacts essentially only the noise figure, which we assume here to be ideal. This assumption is favorable to Arch.2. Nevertheless, we shall see that Arch.1 (the proposed one) is still very competitive from the energy efficiency viewpoint.

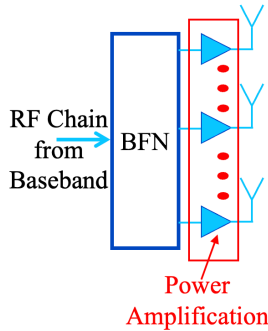


Fig. 8: Arch.2 block diagram. Beamforming network (BFN) consists of amplitude and phase shifters.

From the previously computed link budget in Section IV, we target 0 dB SNR for a cell edge user, given by $\text{SNR}_{\text{rx}} = P_{\text{RF}} G(\phi = 60^\circ, \theta = 26.06^\circ) / (L_{\text{max}} W N_0)$. Plugging in the values from Section IV, we get $P_{\text{RF}} = 20$ dBm. For Arch.1, the AMAF weights, $\mathbf{v}_1 = [0.5, 0.5, 0.5, 0.5]$. Hence, the maximum AMAF PA output power is given by $P_{\text{pa-max}}^{(1)} = \max |v_{1i}|^2 P_{\text{RF}} = -6 \text{ dB} + 20 \text{ dBm} = 14 \text{ dBm} = 25.1 \text{ mW}$. We assume that all the PAs in the (AMAF) array are developed in the same semiconductor technology, and are all biased with the same DC power dictated by the maximum requested RF power. Considering Indium Phosphide (InP) PAs with efficiency $\eta = 0.3$ [11], [12], the Arch.1 DC power consumption, $P_{\text{DC}}^{(1)} = N_a P_{\text{pa-max}}^{(1)} / \eta = 4 \times 25.1 \text{ mW} / 0.3 = 0.33 \text{ W}$. Likewise, for Arch.2, $P_{\text{pa-max}}^{(2)} = \max |u_{1i}|^2 P_{\text{RF}} = -14.65 \text{ dB} + 20 \text{ dBm} = 5.34 \text{ dBm} = 3.42 \text{ mW}$. Thus, Arch.2 DC power $P_{\text{DC}}^{(2)} = N_p P_{\text{pa-max}}^{(2)} / \eta = 2.92 \text{ W}$. We see that the proposed architecture is almost 10x times more power efficient than the baseline.

VI. CONCLUSIONS

We proposed a novel multiuser multibeam architecture with over-the-air active array-based feeding (AMAF) and RIS-based beam steering suited to very high frequency bands. The scheme is based on a fundamental “module” formed by an AMAF-RIS pair, with fixed geometry, and can accommodate any suitable number K of independently steered data streams by stacking such module in a larger array. We demonstrated a design example with (2×2) active antennas at the AMAF and 16×16 passive elements at the RIS. We also demonstrated that there is no dramatic performance loss with practical hardware constraints such as quantized RIS phase shifters (3 bits or more) and beam pointing errors. Our pragmatic design approach is very simple, does not require complicated on-line optimization (unlike most analog-digital multiuser precoding approaches), and can be easily applied to different combinations of AMAF and RIS. The proposed architecture has low hardware complexity (very small number of PAs, simple active beamforming network), and achieves large energy efficiency gains with respect to the baseline active array design with the same beamforming capability.

ACKNOWLEDGMENT

The work of G. Caire was supported by BMBF Germany in the program of “Souverän. Digital. Vernetzt.” Joint Project 6G-RIC (Project IDs 16KISK030).

REFERENCES

- [1] T. S. Rappaport *et al.*, “Wireless Communications and Applications Above 100 GHz: Opportunities and Challenges for 6G and Beyond,” *IEEE Access*, vol. 7, pp. 78 729–78 757, Jun. 2019.
- [2] A. Adhikary *et al.*, “Joint Spatial Division and Multiplexing—The Large-Scale Array Regime,” *IEEE Trans. on Inf. Theory*, vol. 59, no. 10, pp. 6441–6463, Jun. 2013.
- [3] Z. Zhou *et al.*, “Hardware-Efficient Hybrid Precoding for Millimeter Wave Systems With Multi-Feed Reflectarrays,” *IEEE Access*, vol. 6, pp. 6795–6806, 2018.
- [4] V. Jamali *et al.*, “Intelligent Surface-Aided Transmitter Architectures for Millimeter-Wave Ultra Massive MIMO Systems,” *IEEE Open J. of the Commun. Society*, vol. 2, pp. 144–167, 2020.
- [5] K. K. Tiwari *et al.*, “RIS-Based Steerable Beamforming Antenna with Near-Field Eigenmode Feeder,” in *ICC 2023 - IEEE Int. Conf. on Commun.*, May 2023, pp. 1293–1299.
- [6] M. Sadeghian *et al.*, “RIS in Indoor Environments: Benchmarking Against Ambient Propagation,” in *2023 57th Asilomar Conference on Signals, Systems, and Computers*, 2023, pp. 127–133.
- [7] C. A. Balanis, *Antenna Theory, Analysis and Design*. Wiley, 2016.
- [8] S. Venkatesh *et al.*, “A high-speed programmable and scalable terahertz holographic metasurface based on tiled cmos chips,” *Nature Electronics*, vol. 3, no. 12, pp. 785–793, 2020.
- [9] X. Song *et al.*, “Fully-/Partially-Connected Hybrid Beamforming Architectures for mmWave MU-MIMO,” *IEEE Trans. on Wireless Commun.*, vol. 19, no. 3, pp. 1754–1769, Mar. 2020.
- [10] K. Wang *et al.*, “Scheduling and Resource Allocation in 802.11ax,” in *IEEE INFOCOM 2018-IEEE Conf. on Computer Commun.* IEEE, 2018, pp. 279–287.
- [11] H. Wang *et al.* Power Amplifiers Performance Survey 2000-Present. [Online]. Available: <https://ideas.ethz.ch/research/surveys/pa-survey.html>
- [12] J. F. Buckwalter *et al.*, “Fundamental Limits of High-Efficiency Silicon and Compound Semiconductor Power Amplifiers in 100-300 GHz Bands,” *ITU J. on Future and Evolving Technol.*, vol. 2 (2021), no. 7 - Terahertz Commun., pp. 39–50, Oct. 2021.